SCIENCE CHINA
Chemistry

•ARTICLES•

June 2020 Vol.63 No.6: 841–849
https://doi.org/10.1007/s11426-019-9721-0

Electron-transfer enhanced MoO_2-Ni heterostructures as a highly efficient pH-universal catalyst for hydrogen evolution

Benzhi Wang[1], Hexiu Huang[1], Meilin Huang[1], Puxuan Yan[1], Tayirjan Taylor Isimjan[2*] & Xiulin Yang[1*]

[1]*Guangxi Key Laboratory of Low Carbon Energy Materials, School of Chemistry and Pharmaceutical Sciences, Guangxi Normal University, Guilin 541004, China;*
[2]*Saudi Arabia Basic Industries Corporation (SABIC) at King Abdullah University of Science and Technology (KAUST), Thuwal 23955-6900, Saudi Arabia*

Received October 18, 2019; accepted January 7, 2020; published online March 30, 2020

Hydrogen is one of the most promising energy carriers to replace fossil fuels and electrolyzing water to produce hydrogen is a very effective method. However, designing highly active and stable non-precious metal hydrogen evolution electrocatalysts that can be used in universal pH is a huge challenge. Here, we have reported a simple strategy to develop a highly active and durable non-precious MoO_2-Ni electrocatalyst for hydrogen evolution reaction (HER) in a wide pH range. The MoO_2-Ni catalyst exhibits a superior electrocatalytic performance with low overpotentials of 46, 69, and 84 mV to reach −10 mA cm^{-2} in 1.0 M KOH, 0.5 M H_2SO_4, and 1.0 M PBS electrolytes, respectively. At the same time, the catalyst also shows outstanding stability over a wide pH range. It is particularly noted that the catalytic performance of MoO_2-Ni in alkaline solution is comparable to the highest performing catalysts reported. The outstanding HER performance is mainly attributed to the collective effect of the rational morphological design, electronic structure engineering, and strong interfacial coupling between MoO_2 and Ni in heterojunctions. This work provides a viable method for the synthesis of inexpensive and efficient HER electrocatalysts for the use in wide pH ranges.

MoO_2-Ni, pH-universal, electron-transfer, hydrogen evolution, electrolysis

Citation: Wang B, Huang H, Huang M, Yan P, Isimjan TT, Yang X. Electron-transfer enhanced MoO_2-Ni heterostructures as a highly efficient pH-universal catalyst for hydrogen evolution. *Sci China Chem*, 2020, 63: 841–849, https://doi.org/10.1007/s11426-019-9721-0

1 Introduction

Hydrogen produced from water electrolysis is a clean energy carrier with the potential to replace fossil fuels and the water electrolysis is the most economical way of producing hydrogen from the renewable sources [1–4]. However, the cost of hydrogen is still several times higher than that of produced from methane reforming. The price of hydrogen generated from electrolysis is mainly determined by the price of the electricity and the catalysts. A typical electrolyzer is composed of three parts, including electrolytes, catalysts, and membranes [5]. The membrane is selected according to the pH of the electrolyte where the Nafion-based membrane has a similar conductivity but a much higher ion (H^+) exchange rate in the acidic electrolyte than the OH^- ion transport rate of the alkaline membrane (Zirfon filled with a 30 wt% KOH solution), thereof resulting in an higher current density than that of alkaline electrolysis. Besides, due to the low concentrations of freely moving H^+ and OH^- ions in neutral solutions, the overall water splitting usually requires much higher cell voltages. Meanwhile, the H^+ moves much faster than the OH^-. Therefore, the low pH electrolyzer shows a

*Corresponding authors (email: isimjant@sabic.com; xlyang@gxnu.edu.cn)

better energy efficiency than that of the alkaline and neutral electrolyzers. However, the low pH electrolyzer requires noble metal-based catalysts such as Pt and IrO_2 for both anodes and cathodes, respectively. The precious metal catalysts have a high cost and a limited content on the earth's crust, which is not suitable for large-scale applications [6–8]. As a result, finding a low-cost catalyst with better or similar performance as compared to noble metal catalysts is one of the critical steps towards achieving the cheap hydrogen through electrolysis especially in a wide range of pH values. Therefore, intensive efforts have been made to find the earth-abundant materials with HER performances comparable to that of noble metals [9,10].

Heterostructured materials with anisotropic transport properties have been studied extensively in the fields of batteries [11–13], supercapacitors [14,15], and catalysts [16–18]. Moreover, metal-metal(oxide) based hetrostructured materials in particular are used as a high performance catalyst in electrolysis [19,20] and water gas shift reactions [21,22] because of their high durability and unique metal-metal oxide interactions. For instance, Gong *et al*. [23] reported nanoscale $Ni(OH)_2$/Ni heterostructures on the wall of carbon nanotubes that show a similar HER performance to platinum in the alkaline media. Besides, Liu *et al*. [24] demonstrated MoO_2-Ni heterostructure catalysts with a remarkable Pt-like HER activities in alkaline solutions, where the improved HER kinetics is due to the improved hydrogen adsorption resulting from the upraised the O 2p orbital in MoO_2 by the Ni contact. Unique interfacial properties within heterostructures play vital roles in enhancing HER in both cases. Nevertheless, most of the outstanding HER performances of heterostructured catalysts were achieved only in alkaline or acidic solutions. It is worth noting that recent studies on pH-universal catalysts have focused on phosphides [25–27] and precious metals [28,29]. Based on most previous studies [30,31] on Pt catalysts, pH-universal catalysts mainly affect the HER catalytic activity by regulating the hydrogen binding energy between the catalyst and the adsorbed hydrogen. By contrast, little has been done on oxides, mainly because of their chemical instability. However, MoO_2-Ni shows a high stability in both acidic and alkaline solutions due to the layered structure of MoO_2, which was doped by Ni.

Here, we construct a MoO_2-Ni heterostructured catalyst by a controllable three-step approach including electrochemical deposition to prepare Ni/CC, hydrothermal treatment to synthesize Ni-Mo-species/CC, and final calcination to form Ni-MoO_2/CC composites (Figure 1(a)). XPS results demonstrate a strong electronic interaction between Ni and MoO_2 species which resulted in a high HER performance throughout pH range including the acidic pH. The stability under low pH indicates that either Ni was encapsulated by MoO_2 or Ni went into the MoO_2 crystal lattice. Electrochemical studies have shown that the catalyst has a high electrocatalytic activity, a small Tafel slope, a large electrochemical capacitance and a robust stability in universal pH ranges. In addition, the overall water splitting study found that only 1.52 V was required to reach 10 mA cm^{-2} and it is

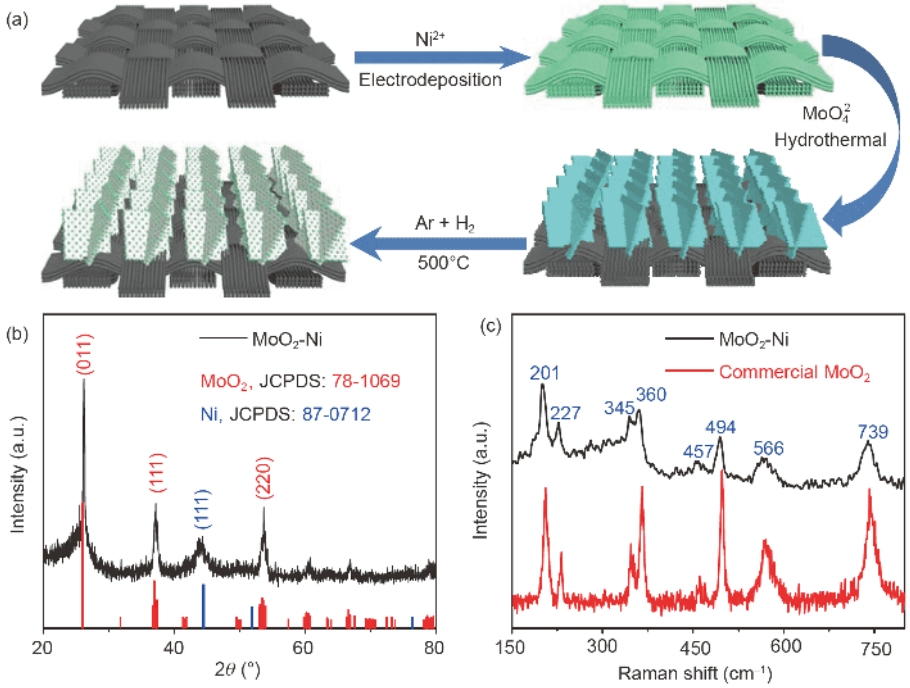

Figure 1 (a) Schematic diagram of the formation of MoO_2-Ni/CC catalysts. (b) XRD pattern of MoO_2-Ni/CC and inset histograms of standard MoO_2 and Ni. (c) Raman spectra of MoO_2-Ni/CC and commercial MoO_2 powder (color online).

far better than most of the currently reported catalysts. Moreover, a detailed catalytic mechanism has been proposed based on the synergy between Ni and MoO_2 species.

2 Experimental

2.1 Materials

Nickel nitrate hexahydrate ($Ni(NO_3)_2·6H_2O$, ≥98%), ammonium molybdate tetrahydrate ($H_{24}Mo_7N_6O_{24}·4H_2O$), thioacetamide ($CH_3CSNH_2$, ≥99%), trimesic acid ($C_9H_6O_6$, 98%), *N*,*N*-dimethylformamide (C_3H_7NO, 99.5%) were analytical reagent and used without further purification. Commercial Pt/C (20 wt% for platinum) was purchased from Alfa Aesar.

2.2 Preparation of Ni-species/CC by electrodeposition

Carbon cloth (CC, 1 cm × 1.5 cm) was ultrasonically cleanized three times to remove impurities in 0.5 M H_2SO_4, ethanol, and H_2O for 5 min, respectively. The Ni-species/CC samples were fabricated by electrodeposition for 1.0 h at −10 mA cm^{-2} in 0.1 M $Ni(NO_3)_2$. These samples were washed with abundant water and air-dried.

2.3 Synthesis of Ni-Mo-species/CC

Molybdate tetrahydrate (240 mg), trimesic acid (42 mg), and thioacetamide (15 mg) were dispersed in 20 mL of H_2O/DMF (*v*/*v*=1/1). The resulting mixture was sonicated to a homogeneous solution. Then, two pieces of Ni-species/CC were put into the above mixture in a glass bottle with a lid and heated to 80 °C for 12 h. After cooling to room temperature, the two samples were taken out, rinsed with plenty of water, and dried in air. The resulting samples were nominated as Ni-Mo-species/CC (Figure S1(a)).

For comparison, we also run a series of controlled experiments. First, the Ni-Mo-species/CC was prepared with adding either trimesic acid or thioacetamide. Second, Ni-species/CC was prepared without the addition of ammonium molybdate tetrahydrate (Figure S1(b)). Third, we failed to prepare Mo-species/CC by immersing fresh CC into the above mixture (Figure S1(c, d)). Therefore, Mo-species/CC material was prepared by directly dropping the ammonium molybdate tetrahydrate aqueous solution onto the CC surface. Fourth, the commercial Pt/C (Johnson Matthey, 20 wt% Pt on the activated carbon) was dispersed in a certain amount of Nafion, H_2O, and ethanol, and then pipetted onto the surface of CC. The theoretical loading was 5.0 mg cm^{-2}.

2.4 Synthesis of MoO_2-Ni/CC

The Ni-Mo-species/CC, Ni-species/CC, and Mo-species/CC were loaded in a porcelain boat and placed in the middle of the tube furnace. Subsequently, the oven was heated to a specific temperature (400, 500, or 600 °C) for 2.0 h in a mixed gas (Ar/H_2) atmosphere. After cooling to room temperature, the obtained samples were named as MoO_2-Ni/CC, Ni/CC, and MoO_2/CC. Note: Ni/CC and MoO_2/CC are only calcined at 500 °C for 2.0 h. The loading of MoO_2-Ni on CC is approximately 10.1 mg cm^{-2} by a delicate balance.

2.5 Characterizations

Scanning electron microscopy (SEM, Quanta FEG 200, Holland) and transmission electron microscopy (TEM, JEOL, JEM-2100F) were used to investigate the morphologies and microstructures of the designed materials. X-ray powder diffraction (XRD) data was detected by a D/Max 2500 V PC with Cu Kα radiation from Rigaku. The chemical states of the samples were examined by X-ray photoelectron spectroscopy (XPS, model: JPS-9010 TR Photoelectron Spectrometer, Japan). Raman spectroscopy was acquired from an inVia confocal Raman microscope (Renishaw, England). The actual loadings of different metals in the catalyst were determined by inductively coupled plasma-atomic emission spectrometry (ICP-AES, IRIS Intrepid II XSP).

2.6 Electrochemical measurements

The electrochemical performance of the as-prepared catalysts was studied by an electrochemical workstation of Biologic VMP3 with a typical three-electrode system in 1.0 M KOH electrolyte. The catalysts modified carbon cloth, graphite plate, and SCE were used as working, counter, and reference electrodes, respectively. Cyclic voltammetry (CV) tests run until achieving a stable electrocatalytic performance of the catalysts at a scan rate of 20 mV s^{-1}. Then, linear sweep voltammetry (LSV) curves were obtained at a low scan rate of 0.5 mV s^{-1}, and electrochemical impedance spectroscopy (EIS) was carried out near the onset potential in the frequency range from 200 kHz to 10 mHz. The long-term stability test was performed at a constant current density of −10 mA cm^{-2} for 36 h in different electrolytes. The use of SCE as a reference electrode to study pH-universal conditions is widely adopted in the literature [32–34]. The SCE reference electrode was also used in this work. To eliminate the possible system error, a standard collaboration, before and after each test, was applied. All potentials (vs. SCE) in this work were calibrated to the RHE by the average CV curves of the two potentials at which the current crossed zero (0.232, 1.040 and 0.649 V) were taken to be the thermodynamic potential in H_2-saturated 0.5 M H_2SO_4, 1.0 M KOH and 1.0 M PBS (Figure S2). The overall water splitting was measured in 1.0 KOH solution with a scan rate of 5 mV s^{-1}.

All reported curves had been corrected by *iR* compensation and all the electrochemical tests were performed at room temperature (25±1 °C).

3 Results and discussion

The X-ray diffraction (XRD) patterns are used to study the crystal structures of MoO_2-Ni/CC, Ni/CC, and MoO_2/CC. As shown in Figure 1(b), the diffraction peaks of MoO_2-Ni/CC synthesized at 500 °C, and MoO_2/CC synthesized by the hydrothermal method (Figure S1(d)) are consistent with the standard MoO_2 (JCPDS: 78-1069) and Ni (JCPDS: 87-0712), respectively. Meanwhile, MoO_2/CC and Ni/CC prepared in control experiments also show high crystallinity (Figure S3). It is noteworthy that no diffraction peaks of MoO_2 were observed without the Ni pretreatment, indicating that the electrodeposited Ni species is a prerequisite for the co-growth of MoO_2-Ni composites on CC. Besides, the MoO_2-Ni/CC composites become more crystalline with the increased calcination temperature (Figure S4(a)). Moreover, the precursors have a negligible effect on the crystallinity of as prepared MoO_2-Ni/CC (Figure S5(a)). Figure 1(c) shows the Raman spectra of MoO_2-Ni/CC and commercial MoO_2 powder, where there are eight distinct MoO_2 characteristic peaks in the range of 150 to 750 cm^{-1} [35,36]. These unique Raman characteristic peaks are also observed in MoO_2-Ni/CC composites synthesized at different calcination temperatures (Figure S4(b)) using different precursors (Figure S5(b)).

The morphology and microstructure of the materials were investigated by SEM and TEM, which shows that the sheet-like Ni species array grows vertically on the CC surface and creates large pores between the nanosheets (Figure 2(a)). After the hydrothermal reaction and calcination at 500 °C, the TEM image shows that the 2D structural porous MoO_2-Ni composite is mainly composed of a large number of particulate materials (Figure 2(b)). The high-resolution TEM image shows clear lattice fringes with lattice spacings of 0.34 and 0.20 nm corresponding to the (011) crystal plane of MoO_2 and the (111) crystal plane of Ni, respectively (Figure 2(c)) [37,38]. The high-angle annular dark-field (HAADF) TEM element mappings indicate that Ni, Mo, and O are uniformly distributed throughout the structure of MoO_2-Ni composites. Besides, the inductively coupled plasma atomic emission spectroscopy (ICP-AES) results show that the mass fractions of Mo and Ni are 23.2 and 39.6 wt% in the MoO_2-Ni composites, and the molar ratio of Mo/Ni is ca. 1/2.79 (Table S1).

The surface composition and chemical states of MoO_2/CC were further analyzed by XPS, which confirmed the presence of Mo, Ni, O, and C elements in MoO_2-Ni/CC (Figure S6(a)). The high-resolution C 1s spectrum is fitted to four peaks, including C=C (284.0 eV), C–C (284.8 eV), C–O (286.0 eV), and C=O (288.0 eV) as shown in Figure S6(b) [39,40]. Generally, the binding energy is inversely related to the surface electron density [41]. Therefore, electron transfer can also be reflected by XPS measurements [24]. As shown

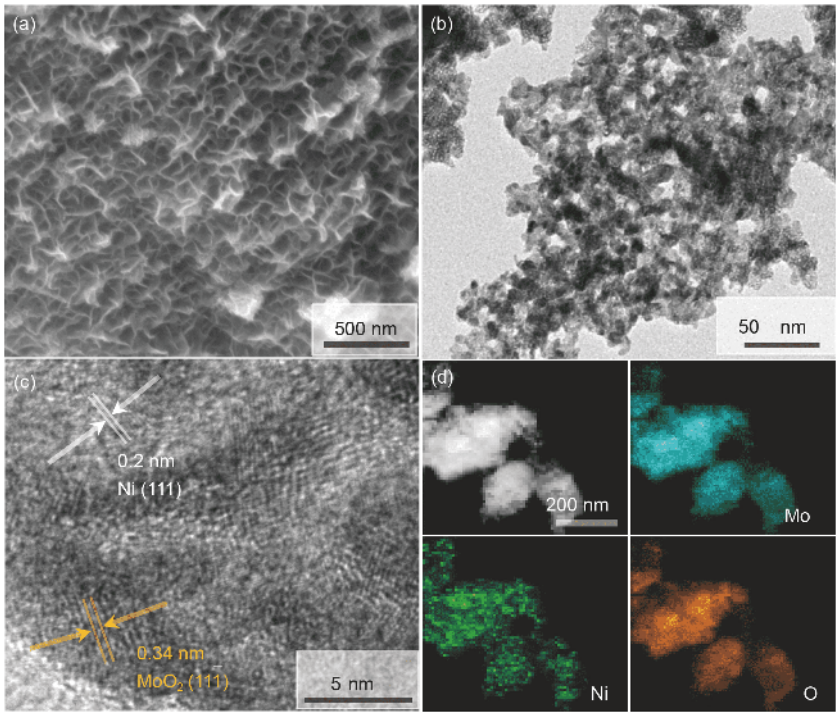

Figure 2 SEM images of (a) Ni-species/CC, (b) TEM image and (c) high-resolution TEM image of MoO_2-Ni/CC. (d) HAADF TEM image and elemental mappings of MoO_2-Ni/CC (color online).

in Figure 3(a), the Mo 3d region of MoO_2-Ni/CC presents two pairs of peaks, where the binding energies at 229.0 and 230.3 eV attribute to Mo^{4+} species, and the binding energies at 231.9 and 235.0 eV correspond to Mo^{6+} species [42]. The Mo $3d_{5/2}$ of MoO_2-Ni/CC negatively shifts about 1.3 eV relative to that of MoO_2/CC (230.2 eV) [38]. Furthermore, the high-resolution Ni $2p_{3/2}$ spectra of MoO_2-Ni/CC are deconvoluted to four peaks at 852.6, 855.8, 857.6, and 862.0 eV (Figure 3(b)), which corresponds to metallic Ni, Ni^{2+}, Ni^{3+} and satellite peaks, respectively [43,44]. Meanwhile, the binding energy of the Ni^{2+} species in MoO_2-Ni/CC has a positive shift of 1.1 eV relative to that of Ni/CC (854.7 eV). These apparent shifts of the binding energies suggest a strong interaction between MoO_2 and Ni species in the MoO_2-Ni/CC composite, which is also an indicator of the electron transfer from Ni species to Mo species through the interface [45]. The strong interaction is presumed to play an important role in promoting the electrochemical hydrogen production.

The HER electrocatalytic activity of MoO_2-Ni/CC was initially optimized by changing the calcination temperature. The results show that the catalyst obtained at a calcination temperature of 500 °C has the best HER activity and the minimum Tafel slope in the whole pH range (Figure S7). Besides, we also explored the effects of different precursors on catalytic performances. It was found that the simultaneous introduction of trimesic acid and thioacetamide can promote HER activities and reduce the charge transfer resistance (R_{ct}) in alkaline solutions (Figure S8). The calcination temperatures and the precursor selection could change the crystallinity and morphology of the catalyst and thereof affect the HER performance significantly.

The electrocatalytic activity of the optimized MoO_2-Ni/CC catalyst with MoO_2/CC, Ni/CC, and commercial Pt/C was first studied in 1.0 M KOH (Figure 4(a)). With the increase of overpotentials, the cathode current density of MoO_2-Ni/CC increased rapidly, indicating that MoO_2-Ni/CC is a high-performance catalyst for the hydrogen production. At a geometric current density of –10 mA cm^{-2}, the overpotential of the prepared MoO_2-Ni/CC electrode is only 46 mV, which is comparable to commercial Pt/C (49 mV), while significantly higher than those of Ni/CC (222 mV), and MoO_2/CC (336 mV). Notably, the catalytic performance of MoO_2-Ni/CC is also superior to most of the previously reported non-precious metal catalysts under alkaline conditions (Table S2). Similar trends in the HER catalytic activity are also reflected in the electrochemically active surface area (ECSA) normalized current density of different catalysts (Figure S9). Tafel slope is commonly used to assess the reaction kinetics and rate determination steps in the HER process. As presented in Figure 4(b), the Tafel slopes of MoO_2-Ni/CC, MoO_2/CC, and Ni/CC were calculated to be 56.9, 90.8, and 93.0 mV dec^{-1}, respectively, indicating that the Volmer-Heyrovsky reaction pathway with the electrochemical desorption of hydrogen is the rate-determining step in alkaline solutions [46,47]. It is worth noting that the MoO_2-Ni/CC has a smaller Tafel slope than all control catalysts, implying a faster kinetic rate of the discharging reaction [48]. Also, the current exchange density (j_0) was calculated by extrapolating the Tafel slope (Figure S10), which also reveals that the MoO_2-Ni/CC has a better intrinsic catalytic activity than those of the rest. At the same time, the MoO_2-Ni/CC also showed the lowest R_{ct} (Figure 4(c)), meaning the MoO_2-Ni composite has higher conductivity to promote the charge transfer, thereby supporting higher HER performances [49].

Generally, the electrochemical double-layer capacity (C_{dl}) is proportional to the ECSA of the catalyst. The C_{dl} can be calculated using cyclic voltammetry (CV) curves in the non-Faraday region (Figure S11). As shown in Figure 4(d), the C_{dl} value of MoO_2-Ni/CC is 465.8 mF cm^{-2}, which is much higher than that of MoO_2/CC (28.3 mF cm^{-2}) and Ni/CC (14.4 mF cm^{-2}), indicating that the MoO_2-Ni/CC has more available active sites [50]. Meanwhile, the turnover fre-

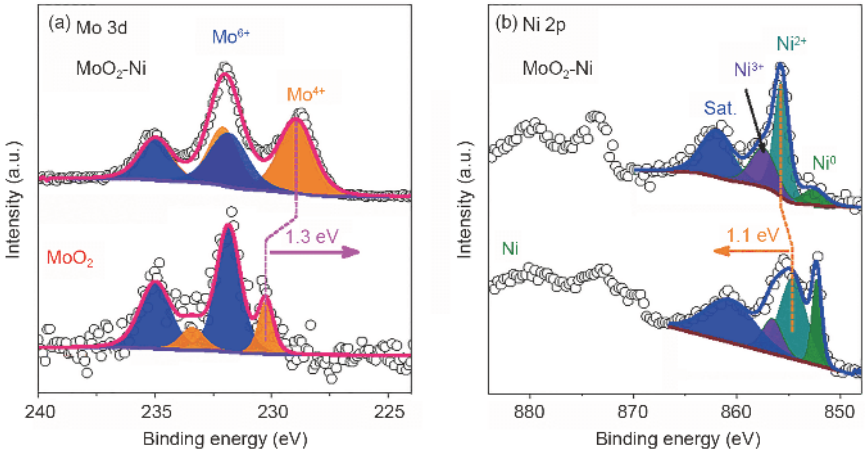

Figure 3 High-resolution XPS spectra of (a) Mo 3d and (b) Ni 2p regions from MoO_2-Ni/CC, Ni/CC and MoO_2/CC, respectively (color online).

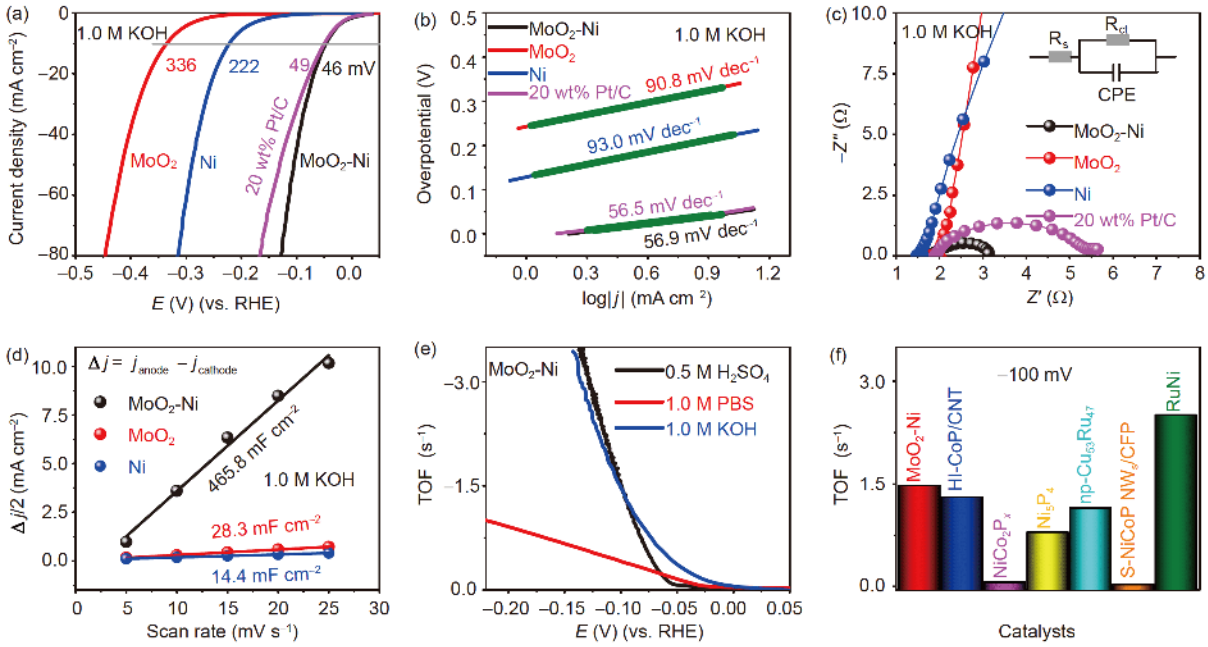

Figure 4 (a) LSV polarization curves, (b) corresponding Tafel slopes, (c) Nyquist plot, and (d) summarized double layer capacitance (C_{dl}) of MoO_2-Ni/CC, MoO_2/CC, Ni/CC and 20 wt% Pt/C in 1.0 M KOH. (e) The turnover frequency (TOF) profiles versus potentials of MoO_2-Ni/CC catalyst in 0.5 M H_2SO_4, 1.0 M PBS and 1.0 M KOH, respectively. (f) Comparison the TOF values with previously reported catalysts at −100 mV in 1.0 M KOH (color online).

quency (TOF) was further used to assess the number of H_2 molecules evolved per second per active site. The TOF is the direct indicator of evaluating the intrinsic activity of an electrocatalyst [25]. Using ICP results to calculate TOF is a widely practiced approach in this type of catalytic systems [1,51,52]. However, it could underestimate the number of the active site on the surface. To have a fair comparison with literature reports, a similar approach was used in this work. As shown in Figure 4(e), the TOF value of MoO_2-Ni/CC rises rapidly when the applied potential increases under acidic, alkaline, and neutral conditions. In 1.0 M KOH, the TOF was calculated to be 1.47 s^{-1} at an overpotential of 100 mV, which is higher than most previously reported catalysts (Figure 4(f), Table S3). Under the same overpotential, the TOF of MoO_2-Ni/CC in 1.0 M PBS and 0.5 M H_2SO_4 was 0.42 and 1.50 s^{-1}, respectively. These high TOF values indicate that MoO_2-Ni/CC can effectively promote the reaction in a given time under all conditions, which is the inherent reason for excellent performances at universal pH [25].

The MoO_2-Ni/CC catalyst also shows excellent HER activity under acidic and neutral conditions. Figure 5a shows the polarization curves of MoO_2-Ni/CC, MoO_2/CC and 20 wt% Pt/C in 0.5 M H_2SO_4. Since Ni can be dissolved in a strongly acidic solution, the catalytic performance of the control Ni/CC has not been studied. The overpotential at 10 mA cm^{-2} of MoO_2-Ni/CC is only 69 mV, which is obviously lower than that of MoO_2/CC (238 mV) and many other transition metal catalysts (Table S4). As shown in Figure 5(b), the Tafel slope of MoO_2-Ni/CC of (31.0 mV dec^{-1}) is the smallest except the state-of-the-art Pt/C (30.1 mV dec^{-1}), demonstrating that MoO_2-Ni/CC has faster kinetics than those of the rest [53]. Figure 5(c) show that the overpotential of MoO_2-Ni/CC at 10 mA cm^{-2} in 1.0 M PBS solutions (pH 7) is only 84 mV, much smaller than MoO_2/CC (359 mV) and Ni/CC (332 mV), and better than most of the reported non-precious metal catalysts (Table S5). Moreover, the MoO_2-Ni/CC has a Tafel slope of 75.3 mV dec^{-1}, lower than that of MoO_2/CC (108.8 mV dec^{-1}) and Ni/CC (150.6 mV dec^{-1}). Long-term stability is another critical factor for evaluating catalyst performances. As shown in Figure 5(e), the MoO_2-Ni/CC exhibits a good catalytic stability for the HER in alkaline solutions, with only decay of about 4.1%. However, it declined by about 25.2% and 25.1% in acidic and neutral solutions, respectively. The stability of Ni-MoO_2 in acidic media could be because Ni is uniformly doped into MoO_2 crystal lattice, and no free Ni is available in any form in the catalyst. The decrease of the HER activity during the stability test is mainly ascribed to the deterioration of the catalyst morphology, crystallinity (Figure S12) and chemical states (Figure S13).

Based on the results above, it can be reasonably inferred that the MoO_2-Ni/CC is a highly active HER catalyst. To further evaluate the catalytic activity, we performed the two-electrode electrolyzed water splitting with RuO_2/CC as the anode and MoO_2-Ni/CC as the cathode (Figure 6(a)). Meanwhile, a large number of bubbles are generated on the surfaces of the two electrodes during the reaction. Notably,

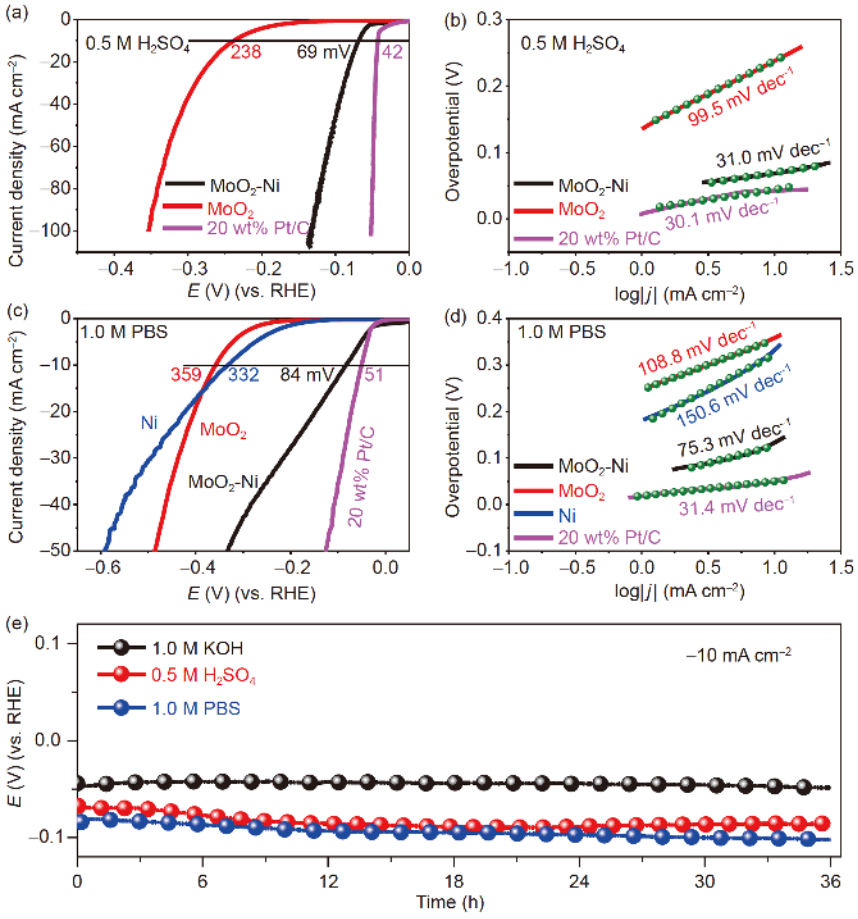

Figure 5 (a) LSV polarization curves, (b) corresponding Tafel slopes of MoO_2-Ni/CC, MoO_2/CC and 20 wt% Pt/C in 0.5 M H_2SO_4. (c) LSV polarization curves, (d) corresponding Tafel slopes of MoO_2-Ni/CC, MoO_2/CC, Ni/CC and 20 wt% Pt/C in 1.0 M PBS. (e) Durability tests of MoO_2-Ni/CC at −10 mA cm^{-2} in 1.0 M KOH, 0.5 M H_2SO_4 and 1.0 M PBS (color online).

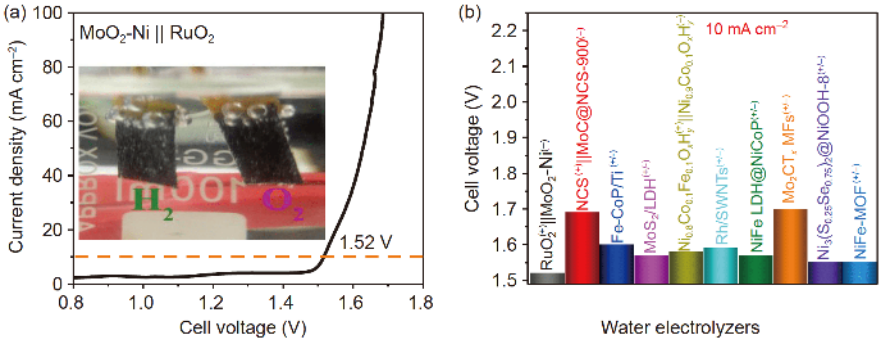

Figure 6 (a) The two-electrode polarization curve of MoO_2-Ni/CC as a cathode and RuO_2/CC as an anode for overall water splitting. (b) Comparison the cell voltages of the currently available electrolytic cells at 10 mA cm^{-2} in 1.0 M KOH (color online).

the two-electrode LSV polarization curve shows that only a potential of 1.52 V is required to reach −10 mA cm^{-2}, which is among the list of the high performing reported catalysts in the alkalized two-electrode system (Figure 6(b), Table S6).

As we discussed above, excellent HER activity is due to the unique heterojunction and the strong synergistic effect through the Ni and MoO_2 interface. The shift in binding energies, as shown in XPS (Figure 3), demonstrates the electron transfer effect between MoO_2 and Ni species, resulting in partially negative and positive charges on MoO_2 and Ni, respectively. In the alkaline and neutral environment, the positively charged Ni species can adsorb H_2O molecules at the interface and synergistically promote the dissociation of H_2O, thereby forming an active intermediate for adsorbing hydrogen on the surface of MoO_2 species (M–H_{ad}) (Scheme 1). The created M–H_{ad} can further bind to one electron and

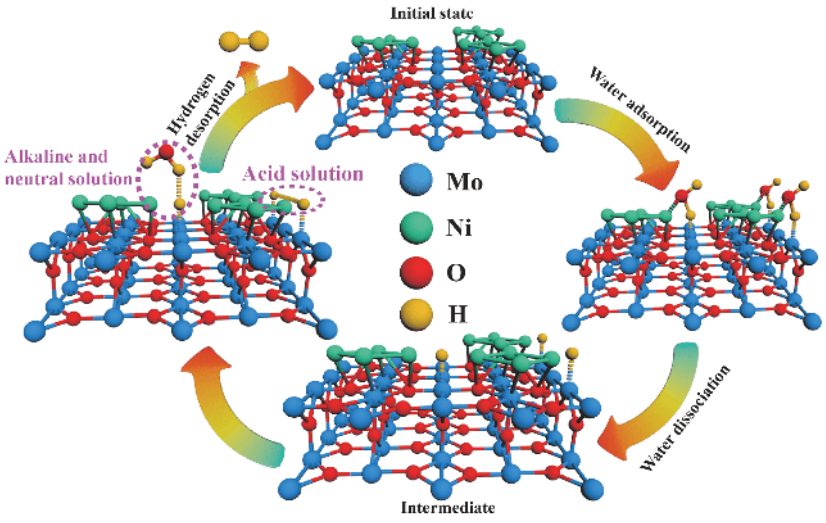

Scheme 1 Schematic diagram of HER catalytic mechanism of MoO_2-Ni/CC catalysts in an alkaline, neutral and acid solution (color online).

more H_2O molecules, and simultaneously release H_2 through the Heyrovsky step ($M–H_{ad} + e^- + H_2O \rightarrow M + H_2 + OH^-$) [54]. It is important to note that the HER in an acidic solution is dominated by the Tafel recombination step ($M–H_{ad} + M–H_{ad} \rightarrow 2M + H_2$) [53].

4 Conclusions

In summary, we constructed a MoO_2-Ni heterostructure by the simple electrodeposition and hydrothermal methods. The optimal MoO_2-Ni exhibits a Pt-like HER activity with a low overpotential of 46, 69 and 84 mV at −10 mA cm^{-2} in 1.0 M KOH, 0.5 M H_2SO_4 and 1.0 M PBS electrolytes, respectively. Besides, the MoO_2-Ni heterostructured electrocatalyst exhibited a high durability in the full pH range for nearly 36 hours. The high HER activity and the long term stability are attributed to the synergy between MoO_2 and Ni, which enhances the electronic interaction between MoO_2 and Ni species through MnO_2 and Ni interface. As a result of the effective charge transfer from Ni to MoO_2, it increases the water adsorption on the catalyst surface and thereof promotes the HER. It is worth to note that catalyst stability in acidic solutions indicates that the Ni species mast has capsulated by MoO_2.

Acknowledgements This work has been supported by the National Natural Science Foundation of China (21965005), Natural Science Foundation of Guangxi Province (2018GXNSFAA294077 and 2018GXNSFAA281220), Project of High-Level Talents of Guangxi (F-KA18015 and 2018ZD004).

Conflict of interest The authors declare that they have no conflict of interest.

Supporting information The supporting information is available online at http://chem.scichina.com and http://link.springer.com/journal/11426. The supporting materials are published as submitted, without typesetting or editing. The responsibility for scientific accuracy and content remains entirely with the authors.

1 Lai J, Huang B, Chao Y, Chen X, Guo S. *Adv Mater*, 2019, 31: 1805541
2 Shi Y, Zhou Y, Yang DR, Xu WX, Wang C, Wang FB, Xu JJ, Xia XH, Chen HY. *J Am Chem Soc*, 2017, 139: 15479–15485
3 Song F, Li W, Yang J, Han G, Liao P, Sun Y. *Nat Commun*, 2018, 9: 4531
4 Zhou P, He J, Zou Y, Wang Y, Xie C, Chen R, Zang S, Wang S. *Sci China Chem*, 2019, 62: 1365–1370
5 Elbert K, Hu J, Ma Z, Zhang Y, Chen G, An W, Liu P, Isaacs HS, Adzic RR, Wang JX. *ACS Catal*, 2015, 5: 6764–6772
6 Chen Z, Song Y, Cai J, Zheng X, Han D, Wu Y, Zang Y, Niu S, Liu Y, Zhu J, Liu X, Wang G. *Angew Chem Int Ed*, 2018, 57: 5076–5080
7 Zhou M, Weng Q, Popov ZI, Yang Y, Antipina LY, Sorokin PB, Wang X, Bando Y, Golberg D. *ACS Nano*, 2018, 12: 4148–4155
8 Li J, Chen J, Wang Q, Cai WB, Chen S. *Chem Mater*, 2017, 29: 10060–10067
9 Chen J, Liu J, Xie JQ, Ye H, Fu XZ, Sun R, Wong CP. *Nano Energy*, 2019, 56: 225–233
10 Liu B, Huo L, Gao Z, Zhi G, Zhang G, Zhang J. *Small*, 2017, 13: 1700092
11 Liu X, Li W, Zou S. *J Mater Chem A*, 2018, 6: 17067–17074
12 Saat G, Balci FM, Alsaç EP, Karadas F, Dag Ö. *Small*, 2018, 14: 1701913
13 Yang ZD, Chang ZW, Xu JJ, Yang XY, Zhang XB. *Sci China Chem*, 2017, 60: 1540–1545
14 Zhang C, Hou M, Cai X, Lin J, Liu X, Wang R, Zhou L, Gao J, Li B, Lai L. *J Mater Chem A*, 2018, 6: 15630–15639
15 Wang M, Li Z, Wang C, Zhao R, Li C, Guo D, Zhang L, Yin L. *Adv Funct Mater*, 2017, 27: 1701014
16 Zhou M, Liu Z, Song Q, Li X, Chen B, Liu Z. *Appl Catal B-Environ*, 2019, 244: 188–196
17 Chen L, Zhang J, Ren X, Ge R, Teng W, Sun X, Li X. *Nanoscale*, 2017, 9: 16632–16637
18 Zhang ZS, Fu XP, Wang WW, Jin Z, Song QS, Jia CJ. *Sci China Chem*, 2018, 61: 1389–1398
19 Qi J, Zhang W, Cao R. *Chem Commun*, 2017, 53: 9277–9280
20 Ji D, Peng L, Shen J, Deng M, Mao Z, Tan L, Wang M, Xiang R, Wang J, Shah SSA. *Chem Commun*, 2019, 55: 3290–3293
21 Kauppinen MM, Melander MM, Bazhenov AS, Honkala K. *ACS Catal*, 2018, 8: 11633–11647

22 Yan H, Qin XT, Yin Y, Teng YF, Jin Z, Jia CJ. *Appl Catal B-Environ*, 2018, 226: 182–193
23 Gong M, Zhou W, Tsai MC, Zhou J, Guan M, Lin MC, Zhang B, Hu Y, Wang DY, Yang J, Pennycook SJ, Hwang BJ, Dai H. *Nat Commun*, 2014, 5: 4695
24 Liu X, Ni K, Niu C, Guo R, Xi W, Wang Z, Meng J, Li J, Zhu Y, Wu P, Li Q, Luo J, Wu X, Mai L. *ACS Catal*, 2019, 9: 2275–2285
25 Zhang R, Wang X, Yu S, Wen T, Zhu X, Yang F, Sun X, Wang X, Hu W. *Adv Mater*, 2017, 29: 1605502
26 Adam A, Suliman MH, Siddiqui MN, Yamani ZH, Merzougui B, Qamar M. *ACS Appl Mater Interfaces*, 2018, 10: 29407–29416
27 Lu XF, Yu L, Lou XWD. *Sci Adv*, 2019, 5: eaav6009
28 Mahmood J, Li F, Jung SM, Okyay MS, Ahmad I, Kim SJ, Park N, Jeong HY, Baek JB. *Nat Nanotech*, 2017, 12: 441–446
29 Yao RQ, Zhou YT, Shi H, Zhang QH, Gu L, Wen Z, Lang XY, Jiang Q. *ACS Energy Lett*, 2019, 4: 1379–1386
30 Zheng J, Sheng W, Zhuang Z, Xu B, Yan Y. *Sci Adv*, 2016, 2: e1501602
31 Sheng W, Zhuang Z, Gao M, Zheng J, Chen JG, Yan Y. *Nat Commun*, 2015, 6: 5848
32 Li Q, Zou X, Ai X, Chen H, Sun L, Zou X. *Adv Energy Mater*, 2018, 1803369
33 Mishra IK, Zhou H, Sun J, Qin F, Dahal K, Bao J, Chen S, Ren Z. *Energy Environ Sci*, 2018, 11: 2246–2252
34 Yao Q, Huang B, Zhang N, Sun M, Shao Q, Huang X. *Angew Chem Int Ed*, 2019, 58: 13983–13988
35 Kumar P, Singh M, Reddy GB. *Mater Res Express*, 2017, 4: 036405
36 Ku JH, Jung YS, Lee KT, Kim CH, Oh SM. *J Electrochem Soc*, 2009, 156: A688
37 Li Z, Yu C, Wen Y, Gao Y, Xing X, Wei Z, Sun H, Zhang YW, Song W. *ACS Catal*, 2019, 9: 5084–5095
38 Yang L, Yu J, Wei Z, Li G, Cao L, Zhou W, Chen S. *Nano Energy*, 2017, 41: 772–779
39 Guo J, Wu C, Zhang J, Yan P, Tian J, Shen X, Isimjan TT, Yang X. *J Mater Chem A*, 2019, 7: 8865–8872
40 Guo J, Wang B, Yang D, Wan Z, Yan P, Tian J, Isimjan TT, Yang X. *Appl Catal B-Environ*, 2020, 265: 118584
41 Jin H, Liu X, Jiao Y, Vasileff A, Zheng Y, Qiao SZ. *Nano Energy*, 2018, 53: 690–697
42 Wan J, Wu J, Gao X, Li T, Hu Z, Yu H, Huang L. *Adv Funct Mater*, 2017, 27: 1703933
43 Zhou Y, Huang W, Zhang X, Wang M, Zhang L, Shi J. *Chem Eur J*, 2017, 23: 17029–17036
44 Ito Y, Ohto T, Hojo D, Wakisaka M, Nagata Y, Chen L, Hu K, Izumi M, Fujita J, Adschiri T. *ACS Catal*, 2018, 8: 3579–3586
45 Chi JQ, Chai YM, Shang X, Dong B, Liu CG, Zhang W, Jin Z. *J Mater Chem A*, 2018, 6: 24783–24792
46 Boppella R, Tan J, Yang W, Moon J. *Adv Funct Mater*, 2019, 29: 1807976
47 Yang L, Zeng L, Liu H, Deng Y, Zhou Z, Yu J, Liu H, Zhou W. *Appl Catal B-Environ*, 2019, 249: 98–105
48 Xiao P, Ge X, Wang H, Liu Z, Fisher A, Wang X. *Adv Funct Mater*, 2015, 25: 1520–1526
49 Youn DH, Han S, Kim JY, Kim JY, Park H, Choi SH, Lee JS. *ACS Nano*, 2014, 8: 5164–5173
50 Yang X, Lu AY, Zhu Y, Hedhili MN, Min S, Huang KW, Han Y, Li LJ. *Nano Energy*, 2015, 15: 634–641
51 Qi Y, Zhang L, Sun L, Chen G, Luo Q, Xin H, Peng J, Li Y, Ma F. *Nanoscale*, 2020, 12: 1985–1993
52 Chen YY, Zhang Y, Zhang X, Tang T, Luo H, Niu S, Dai ZH, Wan LJ, Hu JS. *Adv Mater*, 2017, 29: 1703311
53 Yang X, Lu AY, Zhu Y, Min S, Hedhili MN, Han Y, Huang KW, Li LJ. *Nanoscale*, 2015, 7: 10974–10981
54 Li Y, Wang H, Xie L, Liang Y, Hong G, Dai H. *J Am Chem Soc*, 2011, 133: 7296–7299